Early-age and long-term deformations in reinforced slag-based alkali activated concrete

Bezemer, Huibert Jilles; Luković, Mladena

DOI
10.1016/j.conbuildmat.2025.141317

Publication date
2025

Document Version
Final published version

Published in
Construction and Building Materials

Citation (APA)
Bezemer, H. J., & Luković, M. (2025). Early-age and long-term deformations in reinforced slag-based alkali activated concrete. *Construction and Building Materials*, *476*, Article 141317. https://doi.org/10.1016/j.conbuildmat.2025.141317

Construction and Building Materials 476 (2025) 141317

Contents lists available at ScienceDirect

Construction and Building Materials

journal homepage: www.elsevier.com/locate/conbuildmat

Early-age and long-term deformations in reinforced slag-based alkali activated concrete

Huibert Jilles Bezemer [*,1], Mladena Luković [2]

Delft University of Technology, Stevinweg 1, Delft 2628 CN, the Netherlands

ARTICLE INFO

Keywords:
Distributed fiber optical sensors
Reinforced alkali activated concrete
Shrinkage monitoring
Microcrack

ABSTRACT

To enable wide structural application of alkali activated concretes (AACs) as a sustainable alternative to Portland cement concretes (PCCs), it is vital to understand their interaction with steel reinforcement. Even before applying mechanical loading, significant internal loads (strains), originating from cement hydration, changes in temperature and (internal) relative humidity, can be imposed and will affect reinforcement-concrete interaction. Herein, early-age and long-term induced steel strains have been measured on embedded reinforcement bars instrumented with distributed fiber optical sensors (DFOS) in reinforced concrete beams. A GGBFS-based alkali activated concrete (S-AAC) was compared to a reinforced CEM III/B-based concrete (denoted as S-PCC). Both concretes have been fog-cured for 28 days and successively exposed to 20 °C and 55 % relative humidity for a duration of 1 year. By combining bonded and unbonded DFOS strain measurements, mechanical steel strains induced by autogenous and drying shrinkage could be decoupled from temperature effects. DFOS allowed to detect local strain peaks and microcracks and determine microcrack widths along the length of reinforcement bars. Autogenous shrinkage developed rapidly in S-AAC due to the fast polymerization reaction of GGBFS and negligible early-age expansion, leading to 3 times larger shrinkage at 28 days compared to S-PCC. Yet, unlike S-PCC, S-AAC showed a slower development of shrinkage induced deformations than plain S-AAC, indicating that a significant portion of shrinkage in S-AAC is creep. In addition, autogenous shrinkage induced deformations led to microcracking in S-AAC, contributing to a lowered development of steel deformation. Under drying, S-AAC showed a rapid increase in microcrack width without further significant increases in the mean steel deformation. Microscopic images confirmed the presence of more pronounced microcracking in S-AAC compared to S-PCC. These findings are relevant to gain understanding of the long-term behavior of reinforced AACs.

1. Introduction

With the increase in climate change awareness in recent years [1,2], industries are challenged to reduce their carbon footprint. The concrete industry is responsible for 5–8 % of the anthropogenic carbon emissions [3–5]. As majority of these emissions stem from Portland Cement (PC) clinker production, carbon reduction strategies aim at (partially) replacing cement clinker by industrial by-products, such as ground granulated blast furnace slag (GGBFS). Clinker-free concrete can be realized by activation of GGBFS with an alkaline solution [6,7]. Although GGBFS-based alkali activated concretes (AACs) are promising, their wider application is hampered by insufficient understanding of their long-term (structural) behavior. In particular, AAC shrinkage and its effect on the structural behavior is still unclear, while in general, concrete shrinkage could have a significant effect on the cracking behavior and stiffness response of reinforced concrete structures [8–11].

Recent research showed that, GGBFS-based AACs could exhibit up to twelve times higher autogenous shrinkage deformation compared to PC-based concretes (PCCs) [12–15]. Yet, GGBFS-based AACs were reported to have a lower cracking risk than PCCs under isothermal conditions due to their more pronounced visco-elastic behavior (e.g. creep and relaxation) [14]. On the other hand, under semi-adiabatic conditions, GGBFS-based AACs developed only limited compressive stresses by early age expansion, which caused a rapid build-up of tensile stresses and significantly increased their cracking risk [16].

Under drying, GGBFS-based AACs are reported to show more

* Corresponding author.
E-mail addresses: H.J.Bezemer@tudelft.nl (H.J. Bezemer), M.Lukovic@tudelft.nl (M. Luković).
[1] 0000–0003–0198–3216
[2] 0000–0002–9254–6937

https://doi.org/10.1016/j.conbuildmat.2025.141317
Received 30 December 2024; Received in revised form 7 March 2025; Accepted 11 April 2025
Available online 15 April 2025

significant shrinkage compared to PCCs [13,17–20]. Majority of this shrinkage stems from moisture loss, as carbonation is limited in GGBFS-based AACs due to their dense pore structures, high Ca/Si ratio binder and limited consumption of Na^+-ions from pore solutions [21]. The pronounced drying shrinkage in GGBFS-based AACs was attributed to (1) a dense pore structure, (2) lower elastic modulus compared to PCCs and (3) pronounced visco-elastic behavior [12]. Furthermore, GGBFS-based AACs were found to lose chemically bound water from their C-A-S-H-gels under drying, which causes drying-induced self--desiccation [22].

Although the shrinkage mechanisms of GGBFS-based AACs have become better understood, these studies focused primarily on (free) plain concrete shrinkage. In reinforced concrete structures, embedded reinforcement bars restrain concrete shrinkage, which causes tensile stress development and (possibly) cracking of concrete. Due to the visco-elastic behavior of concrete, only part of the plain (material) concrete shrinkage is imposed on reinforcement bars as mechanical strain. Furthermore, drying is a diffusion based process, causing a non-uniform strain distribution in concrete. Hence, it is difficult to determine internal stress development and possible microcracking in reinforced concrete structures from apparent (plain) concrete shrinkage deformations. It would be desired to measure concrete shrinkage induced strains directly on embedded reinforcement bars. However, it has been challenging to develop measurement techniques with sufficient accuracy and spatial resolution [23]. With recent advances in measurement techniques, distributed fiber optic sensing (DFOS) poses to be a viable technique for strain measurements on embedded reinforcement bars. Fiber optic sensors are thin glass wires (125 μm in diameter), which can transmit light pulses. As the light signal travels along the length of the fiber, it scatters. Part of the scattered signal travels through the cladding and gets lost, while the remaining part can be inferred using Optical Frequency Domain Reflectometry (OFDR) to obtain strain and temperature changes along the fiber. There are four types of scattering that occur and can be used in OFDR [24,25]: (1) Rayleigh, (2) Mie, (3) Brillouin and (4) Raman backscattering. For applications that require accurate strain or temperature readings over longer distances (e.g. monitoring of large structures such as pipelines, bridges and railroads over several kilometers), the Brillouin scattering is a viable option due to its high accuracy (up to 20 με) and spatial resolution (up to 5 m) over longer sensing lengths. For applications that require higher accuracy and resolution over a shorter distance, the Rayleigh backscatter is often preferred due to its stronger backscattering signal, which allows for strain measurements with an accuracy of up to 1 με and a spatial resolution of up to 0.65 mm, while being cost-effective. Given its high spatial resolution, it is considered as a quasi-continuous strain measurement, allowing to capture local strain variations, and determine crack widths and bond-stresses. It is so far mostly used under mechanical loads [23,26–28]. Only a limited number of studies have used it to measure (restrained) shrinkage deformations in traditional reinforced concrete [9,10,23,29]. Note, however that, these studies were mainly focused on total shrinkage deformation and did not distinguish between different shrinkage mechanisms, such as autogenous and drying shrinkage. Furthermore, up to the authors knowledge, no studies have used DFOS to measure shrinkage induced deformations in AACs, while their significant free shrinkage deformations and pronounced visco-elastic behavior emphasize the necessity to evaluate shrinkage induced deformations of reinforced GGBFS-based AACs.

The aim of the current study is to investigate the development of shrinkage induced deformations of a reinforced GGBFS-based AAC over time. Reinforced concrete beams had their reinforcement bars instrumented with DFOS, to monitor mechanical steel strains induced by concrete shrinkage over a period of 1 year. A reinforced GGBFS-based PCC was monitored for comparison. Both concretes are fog-cured for 28 days and successively exposed to drying. A method was developed to separate temperature induced strains from autogenous and drying shrinkage induced strains. Local shrinkage induced strain variations were investigated in depth to explore possible microcrack formation and monitor microcrack widths over time. To explain the development of shrinkage induced deformations of the two different concretes, the development of plain concrete compressive strength, elastic modulus and, autogenous and drying shrinkage was monitored.

2. Materials and methods

2.1. Materials and mix designs

Two types of concrete are studied (Table 1): (1) a GGBFS-based alkali activated concrete (denoted as S-AAC) and (2) a CEM III/B-based concrete (denoted as S-PCC) for comparison. The concretes are designed to be comparable in terms of: (1) aggregates (type, volume fraction, distribution), (2) air content, (3) water-to-solid ratio (w/s) and (4) 28th day compressive strength. The specific gravities of GGBFS and CEM III/B are 2890 kg/m^3 and 2950 kg/m^3, respectively. The chemical compositions of the used GGBFS and CEM III/B are shown in Table 2. S-AAC is activated by an alkaline solution, which is made by mixing a sodium hydroxide solution (4 M) and a sodium silicate solution (27.5 wt% SiO_2, 8.25 wt% Na_2O and 64.25 wt% H_2O) in a 1:2.2 wt proportion. The resulting solution has a Na_2O concentration of 4.5 wt% and a silica modulus (n = SiO_2/Na_2O) of 0.95. The alkaline solution is prepared 24 hours prior to casting. S-PCC was prepared with water. No admixtures were used.

To verify the comparability of the concrete mixes, the following fresh and hardened properties have been obtained (Table 3): (1) density according to EN-12350–6 [31], (2) air content measured with a water column meter, following EN-12350–7 [32] and (3) mean compressive strength at 28 days, determined from three 150 mm cubes. A loading rate of 0.6 MPa/s was used for the cube test, following EN-12390–3 [33].

2.2. Plain concrete

2.2.1. Mechanical properties

The development of compressive strength was determined by testing 150 mm cubes at an age of 1,7, 28, 92, 182 and 365 days. A loading rate of 0.6 MPa/s was applied, following EN-12390–3 [33].

The development of the elastic compressive modulus was determined by testing 100 × 100 × 400 mm^3 prisms at an age of 28, 92, 182 and 365 days. A loading rate of 0.1 MPa/s was used and the modulus was determined on the third loading cycle, which ranged from 10 % to 33 % of the mean compressive prism strength, following method B of EN-12390–13 [34]. All experiments were performed in triplicate. Note, both concretes were fog-cured until an age of 28 days and successively exposed to 55 % relative humidity (RH) and 20°C until testing.

2.2.2. Plain concrete shrinkage

Autogenous shrinkage of plain concrete was determined on sealed 100 × 100 × 400 mm^3 prisms. One day after casting the prisms were demolded, sealed and placed in a temperature controlled room at 20°C. Sealing of prisms was done by three layers of plastic foil, followed by two layers of bitumen-aluminum tape. The seal was checked by weight

Table 1
Mix proportions for the studied mixtures.

	S-AAC	S-PCC
Ingredient	(kg/m^3)	(kg/m^3)
GGBFS	400	0
CEM III/B 42.5 N	0	426
Sand (0–4 mm)	787	787
Gravel (4–16 mm)	947	947
Activating solution	200	-
Water	-	165
w/s-ratio	0.38	0.38

Table 2
Chemical composition of used precursors, determined by X-ray fluorescence [30].

[%]	SiO_2	Al_2O_3	CaO	MgO	Fe_2O_3	S	Na_2O	K_2O	TiO	P_2O_5	LOI
GGBFS	35.5	13.5	39.8	8.0	0.6	1.0	0.4	0.5	1.0	0.0	−1.3
CEM III/B 42.5 N	30.0	11.0	45.0	7.0	1.3	1.9	0.4	0.5	0.9	0.6	0.1

Table 3
Fresh and hardened properties of studied mixtures.

	S-AAC	S-PCC
Fresh properties		
Density (kg/m^3)	2348	2327
Air content (%)	2.3	2.2
Hardened properties (28th day)		
Mean compressive strength (MPa)	69.22 (±0.75)	68.36 (±2.09)

measurements over time. Each prism was instrumented with two measurement clocks, one on each non-casted side, measuring deformation of concrete over a 200 mm central distance (Fig. 1). In addition, a thermocouple was cast-in to monitor the heat evolution of concrete and determine its thermal deformation. The latter was determined by assuming that the coefficient of thermal expansion is 10×10^{-6} /°C [35,36]. Autogenous shrinkage of plain concrete was then determined using Eq. (1),

$$\varepsilon_{c,as}(t) = \varepsilon_{tot,sealed}(t) - \varepsilon_T(t) \quad (1)$$

in which $\varepsilon_{c,as}(t)$ is the autogenous shrinkage deformation of plain concrete, $\varepsilon_{tot,sealed}(t)$ is the total measured concrete deformation on sealed prisms and $\varepsilon_T(t)$ is the thermal deformation of concrete. The measurements started 25–26 hours after casting.

Prisms ($100 \times 100 \times 400$ mm^3) for drying shrinkage measurements were demolded 1 day after casting and then fog-cured (>95 % RH) until they reached an age of 28 days. Then they were instrumented with measurement clocks (Fig. 1) and exposed to drying (55 % RH, 20°C). Drying shrinkage was determined using Eq. (2),

$$\varepsilon_{c,ds}(t) = \varepsilon_{c,ts}(t) - \varepsilon_{c,as}(t) \quad (2)$$

in which $\varepsilon_{c,ds}(t)$ is the drying shrinkage of plain concrete and $\varepsilon_{c,ts}(t)$ is the total deformation measured on unsealed prisms. Three replicates were monitored for autogenous shrinkage and drying shrinkage.

2.3. Reinforced concrete

2.3.1. Instrumentation of distributed optical fiber sensors

Concrete shrinkage induced strains of a reinforcement bar were measured in $1900 \times 200 \times 150$ mm^3 reinforced concrete beams (Fig. 2). All beams contained 8 mm diameter ribbed steel bars (B500B). Reinforced concrete beams were cast in molds made from plywood. After casting, the samples were compacted with a vibration needle and then sealed. The samples were demolded 24 hours after casting, placed on plastic pallets and fog-cured (> 95 % RH) up to the age of 28 days. Note, the plastic pallets had an open upper deck, which allowed all surfaces of the beam to be exposed to the environment. After curing, the samples were moved to another room, where they were exposed to a controlled drying environment (55 % RH, 20°C).

Low bend loss optical fibers with a 125 μm cladding and 200 μm chemically bonded coating were installed on the longitudinal ridge of longitudinal reinforcement bars. Note, these types of thinly coated single-mode fibers exhibit minimal slip between the core of the fiber and the host material, which makes them suitable for measuring steep strain gradients [28]. All beams had their central longitudinal bar instrumented with an optical fiber. In addition, one replicate beam had also an additional fiber installed on the outer longitudinal reinforcement bar. The surface of reinforcement bar ridges were prepared by sandpapering and successively cleaned with ethanol. The fibers are continuously bonded with a cyanoacrylate adhesive over the central region of the bar (Fig. 2). After the fibers are bonded, a thin film (i.e. approx. 0.05 mm) of a polyurethane-based coating was applied for protection. Given the its dimension compared to the diameter of the reinforcement bar, it is assumed that this coating thickness does not influence the measurement. Outside the central region, the fibers are unbonded and guided through a protective jacket. A coreless fiber was spliced at the end of the fiber to ensure refraction and termination of the signal. Strain measurements were made at discrete timesteps using Luna Inc. Odisi 6100. For every timestep, 5 measurements were made with a speed of 10 Hz and a spatial resolution of 0.65 mm.

A total of 6 beams per mixture were monitored. 2 beams per mixture were semi-continuously monitored by taking measurements every 5 minutes in the first 24 hours (up to demolding) and later at less

(a) (b)

Fig. 1. (a) Sealed concrete prisms instrumented with a thermocouple and measurement clocks and (b) unsealed concrete prisms instrumented with measurement clocks.

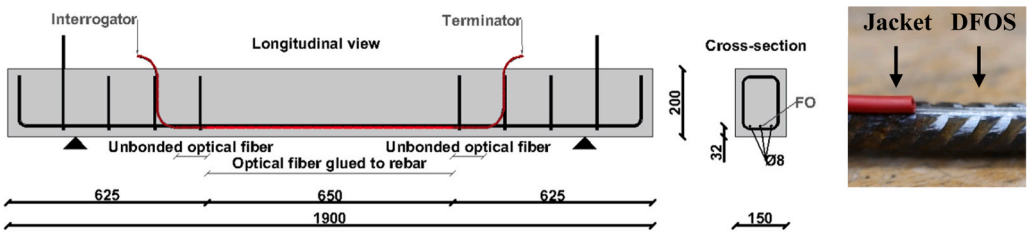

Fig. 2. (a) Specimen layout with embedded DFOS and (b) DFOS instrumented on reinforcement bar. Dimensions are in milimeter.

frequent time intervals. A first (zero-)measurement was made directly after casting (1.5 hour after casting). The remaining 4 beams had their first (zero-)measurement 6 hours after casting and had their second measurement when exposed to drying. Note, for all plain and reinforced concrete samples, time is expressed with respect to the beginning of casting. In order to compare trends from different tests, previously measured deformation is set as a starting point. For example, when plain autogenous shrinkage (measured 26 hours after casting) is compared with autogenous shrinkage deformations in the beams (started 1.5 hour after casting), then plain autogenous shrinkage measured from 26 hours is superimposed to the autogenous shrinkage deformations measured until 26 hours. The number of replicates was reduced at later ages given the low measurement scatter.

2.3.2. *Post-processing of distributed optical fiber sensing data*

To reduce noise and obtain shrinkage induced mechanical strains at the reinforcement, raw strain data was post-processed with an automated MATLAB-script. Firstly, the 5 measurements were averaged per timestep. Secondly, the strain readings were corrected for temperature changes because DFOS are sensitive to both strain and temperature variations. A temperature change causes inherent thermal deformation of the fiber and a change in the refractive index, which can be misinterpreted as imposed strain by the interrogator. For the bonded part of the fiber, it is difficult to distinguish between actual strain and temperature induced spectral shifts. However, for the unbonded part, the fiber is unstrained and a change in the spectral shift is solely caused by a temperature change. Hence, the temperature change in the specimen can be obtained from the unbonded part of the fiber by using Eq. (3):

$$\Delta T(t) = \frac{\bar{\varepsilon}_{unbonded}(t)}{K_\varepsilon} K_T \tag{3}$$

in which ΔT is the temperature change with respect to the zero-measurement; $\bar{\varepsilon}_{unbonded}$ is the mean strain reading for the unbonded part of the fiber; K_ε and K_T are strain and temperature calibration factors of the used fiber, respectively. Approximately 95 % of a temperature induced spectral shift can be attributed to a temperature induced change of the refractive index [37]. Furthermore, given that the coefficient of thermal expansion of steel is significantly larger than that of the optical fiber, using the obtained temperature change (Eq.3), the difference between thermal deformation of the reinforcement bar and the optical fiber is deduced from the measurements to obtain shrinkage induced steel deformation. As the coefficient of thermal expansion of steel is comparable to that of concrete [35,36,38], temperature changes are assumed not to induce differential deformations between steel and concrete, and shrinkage induced strains can be obtained by Eq. (4):

$$\varepsilon_{s,tot}(x,t) = \varepsilon_{measured}(x,t) - (0.95\bar{\varepsilon}_{unbonded}(t) - \Delta T(t) CTE_{fiber})$$

$$\varepsilon_{s,th}(x,t) = \Delta T(t) CTE_{steel}$$

$$\varepsilon_{s,sh}(x,t) = \varepsilon_{s,tot}(x,t) - \varepsilon_{s,th}(x,t) \tag{4}$$

in which $\varepsilon_{s,tot}$ is the total steel deformation; $\varepsilon_{measured}$ is the measured strain of the bonded part of the fiber; CTE_{steel} is the coefficient of thermal expansion of steel, taken as 10×10^{-6} /°C [36,38]; CTE_{fiber} is the coefficient of thermal expansion of the fiber, taken as 0.55×10^{-6} /°C; $\varepsilon_{s,th}$ is the thermal deformation of steel; $\varepsilon_{s,sh}$ is the shrinkage induced steel deformation. Note, it is assumed that the optical fibers are rigidly bonded to the steel; shear lag and interfacial slip are assumed to be negligible. This seems a reasonable assumption considering the thickness of the fibers (200 μm) and the thin layer of glue used, and was confirmed by the presence of local strain variations (local rib-effects) in the unprocessed data. After temperature compensation, only the bonded part of the fiber is further analyzed. Thirdly, similar to [23,28,39,40], an outlier removal filter was used, which removed data that deviated more than 3 times the standard deviation over a moving median with a window length equal to rib-spacing. And lastly, due to the small spatial resolution of DFOS (0.65 mm), DFOS captures local rib-effects stemming from (1) local bond action between concrete and steel and (2) non-uniaxial strain state along the reinforcement bar [28]. The latter is intrinsically related to the geometry of the reinforcement bar and its effect interferes with the local bond action between concrete and steel. This complicates the decoupling procedure and could cause misinterpretation of local strain peaks along the fiber. Hence, similar to [28], local rib effects were removed by down-sampling the strain response to rib-spacing by averaging over the rib-spacing distance, which was 4 mm in the current study. Fig. 3 shows a typical DFOS strain measurement and illustrates the post-processing steps.

Local strain peaks could be observed along the reinforcement bar, which could indicate the presence of microcracks. Previously, the ability of DFOS to detect microcracks was questioned, as strain peaks could as well be caused by differential shrinkage between aggregate and paste [26]. In the current study, three criteria are used to detect microcracks: (1) a low-pass filter is used to allow only strain peaks with a period of more than 1.5 times the maximum aggregate size to pass, (2) a peak prominence filter is used to allow strain variations that passed the low-pass filter and have a prominence of 50 μm/m to be detected as peak and (3) detected peaks are only detected as cracks if the filtered steel strain gradient exceeds 2 μm/m/mm. Similar criteria were shown to be effective for detecting cracks in concrete under mechanical loads [23,39]. Crack widths were determined by integration of unfiltered steel strains over the distance where the steel strain threshold was exceeded (Fig. 4), following Eq. (5),

$$CW(t) = \int_{x_1}^{x_2} \left(\varepsilon_{s,sh}(x,t) - \frac{\varepsilon_{s,sh}(x_1,t) + \varepsilon_{s,sh}(x_2,t)}{2}\right) dx \tag{5}$$

in which CW is the crack width; x_1 is the first location along the reinforcement bar, where the strain threshold was exceeded; x_2 is the last location along the reinforcement bar, where the strain threshold was exceeded. The second term in Eq. (5) accounts for the average concrete deformation between cracks. Note, the low-pass filter is only applied to detect a crack, while unfiltered steel strains are used to determine (micro)crack widths.

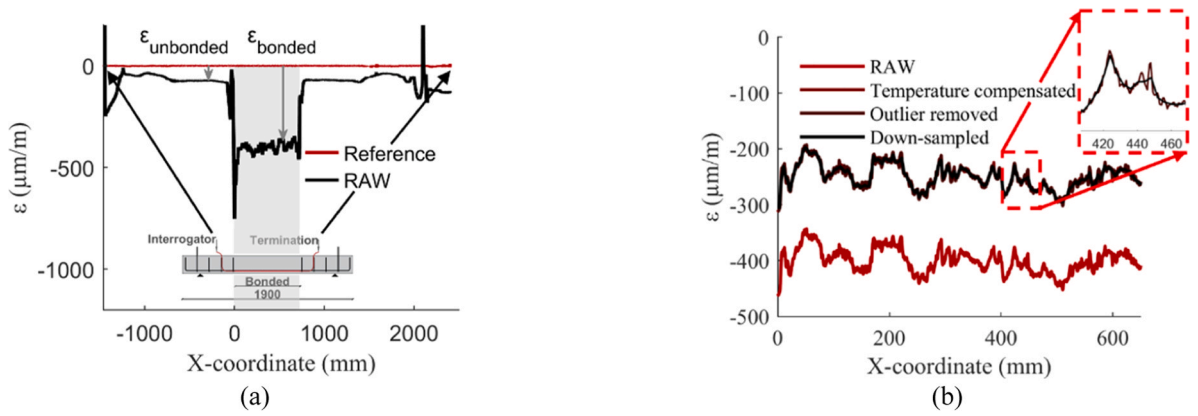

Fig. 3. Post-processing of DFOS data: (a) after temporal averaging and (b) focusing on bonded part: temperature compensated, outlier removed and down-sampled to rib-spacing.

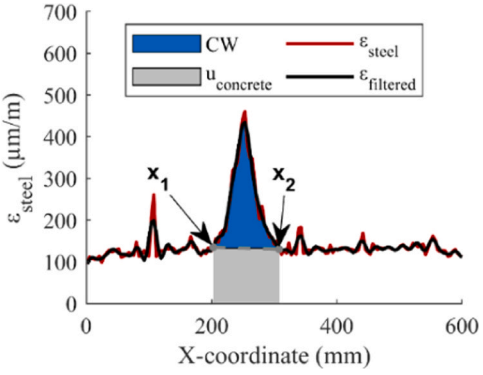

Fig. 4. Crack width calculation from DFOS data.

3. Results & discussion

3.1. Plain concrete shrinkage

Fig. 5a shows the development of plain concrete shrinkage. This figure shows that the autogenous shrinkage of S-AAC developed rapidly in the first 7 days, reaching 190 μm/m, while S-PCC showed a significantly slower development of autogenous shrinkage, reaching 60 μm/m at 7 days. This rapid development of autogenous shrinkage in S-AAC is in line with earlier findings [12–15] and has been attributed to (1) a lower elastic modulus compared to PCCs, (2) significant chemical shrinkage, (3) dense pore size distribution causing high capillary pressure from self-desiccation, (4) refinement of porous structure and (5) pronounced pore pressure induced visco-elastic behavior [16,41–44]. S-AAC shows immediate development of shrinkage, while S-PCC exhibits expansion in the first 48 hours. Early-age expansion is typical for CEM III/B concretes due to the formation of expansive reaction products, such as ettringite [45,46]. Expansive reaction products are limited in GGBFS-based AACs [42], leading to immediate shrinkage deformations. Note, although thermal deformations were obtained from measuring the internal concrete temperature with thermocouples, temperature had little effect on the shrinkage readings as temperature readings did not change more than 1°C after starting the measurements. Another reason for the rapid development of autogenous shrinkage in S-AAC might be its rapid early-age strength development. Fig. 5b shows that S-AAC has a rapid development of compressive strength in the first 7 days. For example, S-AAC reaches already 24 MPa in the first 24 hours and 62 MPa (≈90 % of its 28th day strength) in the first 7 days, while S-PCC only reaches a strength of 13 MPa after 1 day and 47 MPa (≈69 % of its 28th day strength) at 7 days. This is in line with earlier findings from Nedeljkovic et al. [47], who found that GGBFS-based AACs showed rapid early-age strength development due to rapid precipitation of reaction products from its pore solution.

After 7 days, both concretes kept developing autogenous shrinkage reaching 110 and 350 μm/m at 28 days and 190 and 500 μm/m after 6 months for S-PCC and S-AAC, respectively. Fig. 5c shows that the weight change of sealed samples remained below 0.3 % during the whole monitoring period, indicating that proper sealing conditions have been obtained and the measured deformations can be attributed to autogenous shrinkage. Interestingly, the development rate of autogenous shrinkage of S-AAC drops significantly after 3 months and becomes similar to S-PCC. For example, from 28 days to 3 months the average shrinkage development for S-AAC was 1.7 μm/m/day, while this was only 0.7 μm/m/day for S-PCC. From 3 months to 6 months, this rate reduced to 0.4 μm/m/day for both concretes. One reason could be the stagnation of binder polymerization, as S-AAC shows no significant strength gain after 3 months, while it still gained strength from 28 days to 3 months. S-PCC kept, albeit at a slower pace, gaining compressive strength up to 6 months.

Under exposure to drying, S-AAC showed a rapid development of total shrinkage, reaching 925 μm/m at 1 year, while S-PCC had a slower development of total shrinkage, reaching 500 μm/m at 1 year. By subtracting autogenous shrinkage from the total shrinkage, the contribution due to moisture loss to the environment is obtained. Fig. 5a shows that drying shrinkage is more pronounced in S-AAC than in S-PCC and thus that the larger total shrinkage of S-AAC cannot be solely attributed to its more pronounced self-desiccation. For example, after 6 months the drying shrinkage of S-AAC is 40 % larger than in S-PCC. Similar trends have been observed before [13,17–20]. Although the drying shrinkage of S-AAC is larger than S-PCC, S-AAC shows only half of the weight change from S-PCC under drying (Fig. 5c). This is in line with earlier findings [13,41], where the lower weight loss of AAC was attributed to (1) microstructural rearrangement [12] and (2) carbonation shrinkage of AACs under drying [13]. However, note that, carbonation was found to be limited in GGBFS-based AACs due to their dense pore structures, high Ca/Si ratio binder and limited consumption of Na^{+}-ions from pore solutions [21]. Instead, the pronounced drying shrinkage of S-AAC might at least partially be attributed to a reduced elastic modulus, as a softer matrix would cause larger deformations under the same capillary pressure. As can be depicted from Fig. 5d, the elastic compressive modulus of S-AAC was already 10 % lower than that of S-PCC at 28 days and decreases by 25 % from 37 GPa to 28 GPa from 28 days to 1 year, while S-PCC shows, albeit statistically insignificant, a slight increase in elastic modulus from 28 days to 1 year. Similar results have been reported before [11,48,49] and the decreasing elastic modulus of GGBFS-based AACs over time was attributed to microcracking and microstructural rearrangement under drying [11].

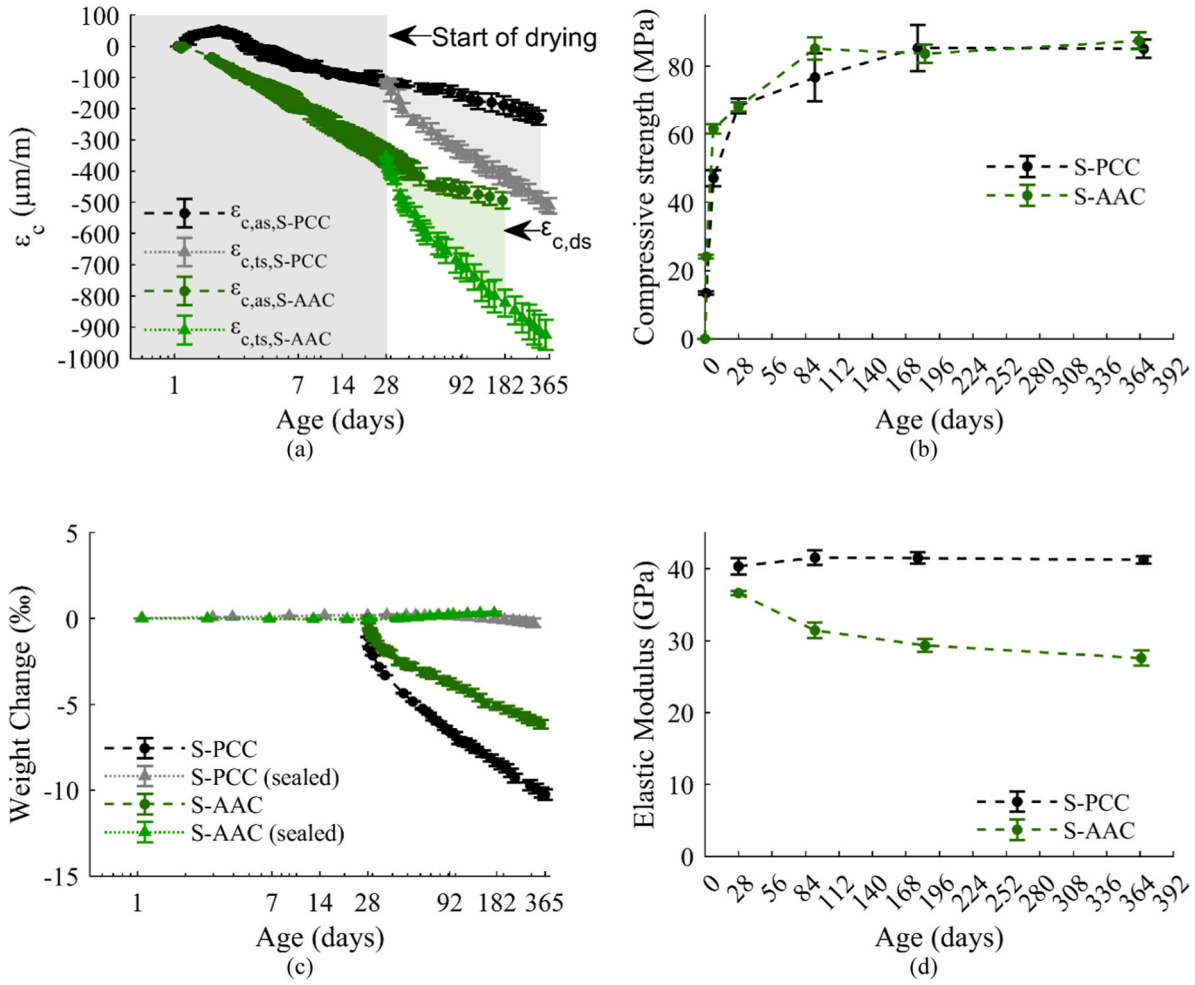

Fig. 5. Development of (a) plain concrete shrinkage, (b) compressive strength, (c) weight change and (d) elastic modulus.

3.2. *Autogenous shrinkage induced deformations*

Fig. 6a shows the development of steel deformations measured by DFOS in the first 672 hours (28 days). Directly after starting the measurements, shrinkage strains developed, reaching approx. 45 μm/m after 6 hours for both concretes. It is unlikely that these strains are induced solely by concrete shrinkage, as at this age concrete would not have been able to develop significant stiffness and bond to transfer deformations to the reinforcement. Significant stiffness (> 2 GPa) was only found 6 hours and 10.5 hours after casting for a similar GGBFS-based AAC [16] and CEM III/B-based concrete [46], respectively. A possible explanation for the development of steel strain in these first hours after casting could stem from plastic flow of concrete and thermal deformation. Note, the total steel deformation shows the net-induced deformation of steel as a competition between thermal deformation of steel, autogenous expansion induced deformations and concrete shrinkage induced deformations. Once the concrete develops significant stiffness, concrete shrinkage starts to induce steel deformations. As can be depicted from the development of total steel deformation, S-PCC develops significant shrinkage deformations only 14 hours after casting. At this point, the temperature of S-PCC is still rising (Fig. 6b). Similarly, S-AAC shows a significant development of steel deformation 9.5 hours after casting, which coincides with the end of its dormant period (Fig. 6b). In the first hour after casting, both concretes have a rapid rise in temperature. However, S-AAC shows a dormant period from 5 to 12 hours, which is when there is hardly any temperature increase, while S-PCC shows no signs of a slower evolution of heat. After 12 hours, S-AAC shows a rapid increase in temperature again, reaching 35°C 22 hours after casting. S-PCC reaches a lower peak temperature of 32°C after casting. Similar heat evolutions were observed by Li et al. [16], where they compared the evolution of heat from their GGBFS-based AAC to an Ordinary Portland Cement Concrete (OPCC) and concluded that GGBFS-based AACs have a lower evolution of heat. Note, in the current study, the concretes are demolded 24 hours after casting and relocated to a fog-room (20°C and >95 % RH). This contributed to a rapid decline in temperature after 24 hours.

Fig. 6c shows the development of autogenous shrinkage induced strains. From this graph it becomes clear that DFOS are capable of capturing the same trend as was observed in plain concrete. S-AAC shows more significant autogenous shrinkage induced deformations, reaching 320 μm/m at 672 hours (28 days), compared to S-PCC, reaching 115 μm/m at 28 days. Furthermore, Fig. 6c shows the comparison between autogenous shrinkage induced deformations and plain concrete shrinkage. It can be observed that the plain shrinkage deformation of S-PCC is almost completely transferred to the reinforcement, indicating that the reinforcement poses a low degree of restraint. Note, as the beams are asymmetrically reinforced, restrained deformations would induce bending and creep effects, but these effects seem to be minor in S-PCC due to the low degree of restraint, at least after 72 hours. In the first 72 hours, autogenous expansion is more significant in plain S-PCC (53 μm/m) than in reinforced S-PCC (22 μm/m). This could possibly be explained by significant creep during the expansive phase and a low concrete-steel bond after 15 hours, preventing autogenous expansion to be transferred to steel. Liang et al. [45] observed that CEM III/B-based concretes can show significant creep during the expansive phase, while it is low during the shrinkage phase. Unlike S-PCC, S-AAC

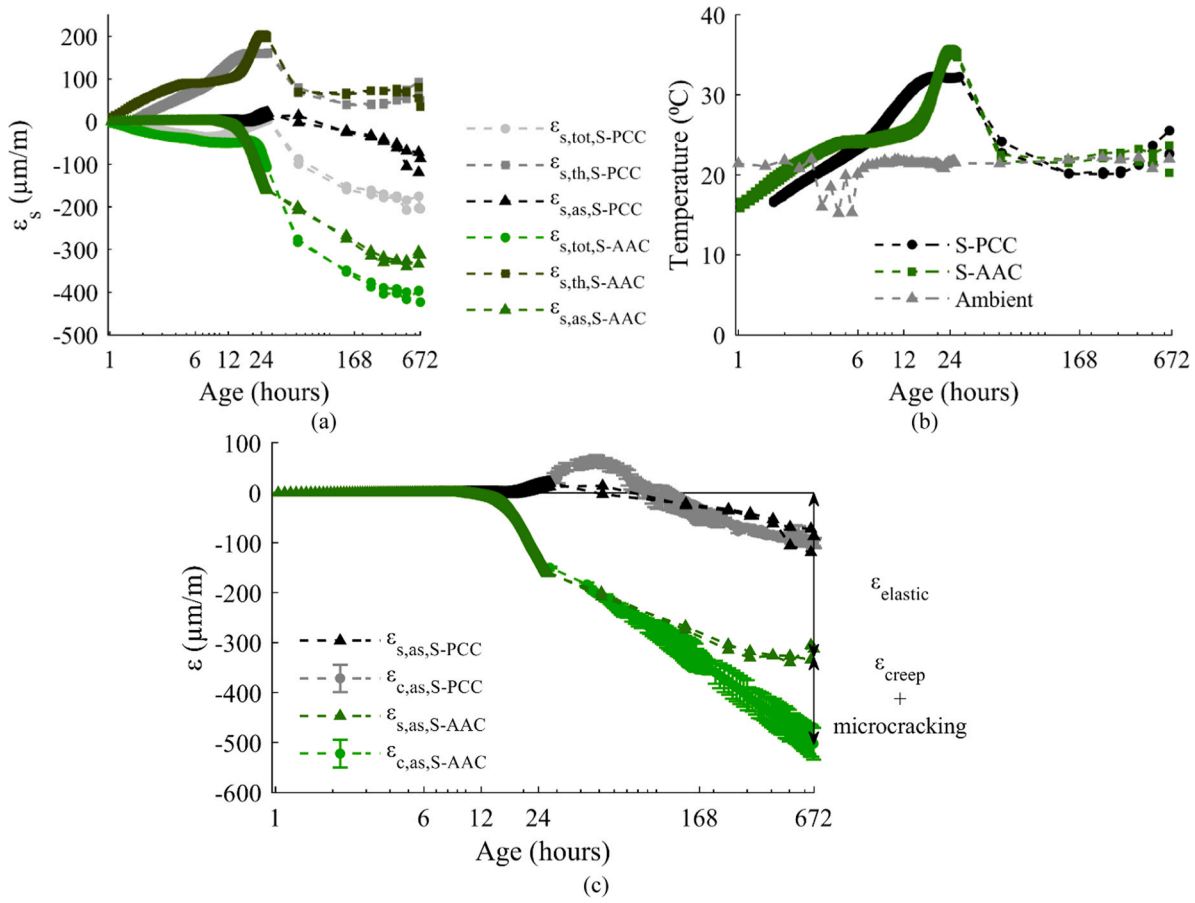

Fig. 6. Development of (a) total ($\varepsilon_{s,tot}$), thermal ($\varepsilon_{s,th}$) and autogenous shrinkage induced deformations ($\varepsilon_{s,as}$), (b) temperature and (c) autogenous shrinkage induced deformation ($\varepsilon_{s,as}$) compared to plain autogenous concrete shrinkage ($\varepsilon_{c,as}$) in the first 672 hours (28 days).

shows a slower development of shrinkage induced deformations compared to its plain concrete shrinkage. The difference between plain and shrinkage induced deformations becomes already apparent after 48 hours and increases over time. After 672 hours, only 64 % of the plain concrete shrinkage is imposed to steel for S-AAC, while this is 95 % for S-PCC. This indicates that a significant portion of the autogenous shrinkage of S-AAC stems from pore pressure induced creep, as plain shrinkage comprises an elastic and a creep part [50–53] and only the elastic part is imposed to steel. More specifically, S-AAC shows a 7 times larger creep ($\varepsilon_{creep}/\varepsilon_{elastic}$) than S-PCC in the first 672 hours. This is in line with findings from Li et al. [14], who found that the early-age creep of GGBFS-based AACs could be 8 times larger than for conventional concretes. This significant early-age creep of GGBFS-based AACs was partially attributed to a reduced stacking regularity of C-A-S-H gels [14], which are mainly formed in GGBFS-based AACs, compared to C-S-H gels, which are mainly formed in OPCCs.

Fig. 7 shows the development of autogenous shrinkage induced deformations along the reinforcement bar for the first 28 days. From this graph it becomes apparent that after 2 days significant strain variations develop in S-AAC, while S-PCC shows less variation in strains along the length of the reinforcement bar. The appearance of these local peaks might be an indication of shrinkage induced microcracking. Note, as the degree of restraint from reinforcement is relatively low in the current study, it might as well be that microcracking is caused by aggregate restraint. Lura et al. [54] showed that in high performance cement-paste autogenous shrinkage can induce microcracks. Consequently, the development of autogenous shrinkage induced microcracking in GGBFS-based AACs was hypothesized and put forward as a possible explanation for degrading mechanical properties [14,49,55]. Yet, these studies could not prove the presence of autogenous shrinkage induced microcracking in AACs. The presence of autogenous shrinkage induced microcracks could, in addition to creep, be another reason for the difference in plain shrinkage and shrinkage induced deformations in S-AACs.

3.3. Drying induced deformations

Fig. 8 shows the continued development of shrinkage induced steel strain along the reinforcement from the onset of drying (55 % RH and 20°C). Although the fibers were installed and treated with care, the optical fiber embedded in one of the S-AAC beams broke in the middle of the beam (Fig. 8b). It was still possible to obtain sufficient backscatter of the signal and measure strains up to the fiber breakage point. Similarly, in one of the S-PCC beams a fiber failed close to the end of the bonded part (Fig. 8f) and strains could only be measured in the first 92 days. Nevertheless, these beams show similar results compared to their replicates and are therefore included in further analysis. From Fig. 8 it becomes apparent that, both concretes continued to develop shrinkage induced strains from 28 days up to the monitoring period of 1 year. Similar to plain concrete shrinkage (Fig. 5a), S-AAC rapidly develops shrinkage induced deformations directly after exposure to drying, while the strain development is more gradual for S-PCC. Furthermore, both concretes show that with time, existing local strain variations are amplified and new peaks are formed, indicating that new microcracks are formed and existing microcracks grow. Note, Fig. 8 shows the combined effect of continued autogenous shrinkage deformation and drying induced deformations, as it was not possible to separate these two. Modelling could be a feasible solution to decouple shrinkage mechanisms and to couple plain concrete shrinkage to shrinkage induced deformations with consideration of size effects in drying, creep

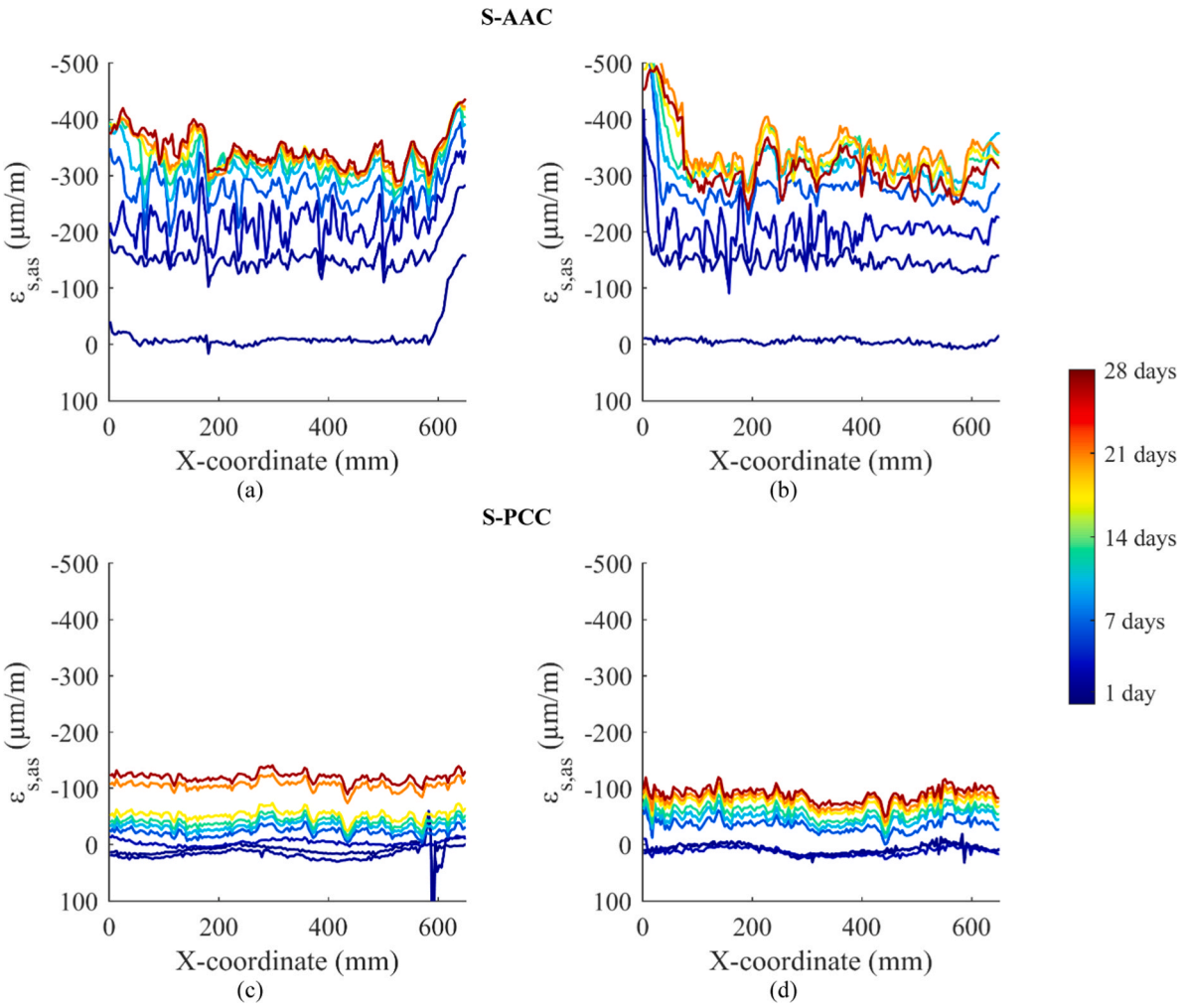

Fig. 7. Development of autogenous shrinkage induced steel strain for S-AAC replicates (a-b) and S-PCC replicates (c-d) in the first 28 days.

deformations and microcracking.

Fig. 9a shows the total development of shrinkage induced deformations. Interestingly, the strain development rate for S-AAC seems to slow down from 56 days and further strain increments are limited. This is not observed for S-PCC nor for the plain concretes (Fig. 5a). As temperature remained relatively constant over time and changes that did occur could be accounted for by the designed DFOS layout, as can be depicted from Fig. 9b, the stagnation in the strain development of S-AAC cannot be attributed to thermal effects. Instead, it could indicate that a significant portion of plain concrete shrinkage of GGBFS-based AACs under drying stems from creep, as GGBFS-based AACs can exhibit twice as high creep compared to OPCCs under drying [56]. However, the plain S-AAC samples were still losing weight after 1 year (Fig. 5c), which indicates that the pore relative humidity of S-AAC has not yet equilibrated with the environment (i.e. there is still a hygral gradient within the sample). For the reinforced concrete beams, which have a larger cross sectional area than the plain concrete samples, it would take even longer for the pore relative humidity to equilibrate with the environment. Hence, the elastic part of drying shrinkage is still developing. The stagnation in the development of shrinkage induced deformations in S-AAC could be caused by (drying induced) microcracking, as GGBFS-based AACs were found to develop microcracks under drying [11,48,57].

Fig. 9c shows the development of maximum crack widths over time and shows that both concretes develop autogenous shrinkage-induced microcracks. For S-AAC, microcracks seem to already form 51 hours after casting, while a first microcrack in S-PCC is only detected after 13 days. Furthermore, crack widths are larger in S-AAC than S-PCC. For example, the maximum crack in S-AAC reaches a width of 4 μm at 28 days, while the maximum crack width is only 0.5 μm in S-PCC. Microcracks were also observed by the eye on the surface of S-AAC at 28 days, but could not be detected for S-PCC. The presence of autogenous shrinkage induced microcracks in S-AAC confirms earlier hypotheses [14,49,55] and can be attributed to the rapid development of autogenous shrinkage in S-AAC. Under drying, the maximum crack width continues to increase, reaching 5 μm and 10 μm for S-PCC and S-AAC, respectively, after 1 year. Fig. 9d shows that the increase in the mean steel strain due to shrinkage correlates with the increase in the average microcrack width. Decreases in mean microcrack width, for increasing steel strain, indicate that new cracks are formed. Decreases in maximum microcrack width indicate that, microcracks can close when adjacent microcracks open. Interestingly, when S-AAC reaches a steel strain of −400 μm/m, the mean crack width continues to increase, while the development of steel strain stagnated. Similarly, after 56 days, which is when the steel strain reaches approx. −400 μm/m, the maximum crack width rapidly increases, indicating that the stagnation of shrinkage induced steel deformation in S-AAC after 56 days might indeed be related to microcracking. Furthermore, this could possibly explain the observed reduction in stiffness, tension stiffening and cracking load in reinforced GGBFS-based AAC members over time [11].

Both concretes had one reinforced concrete beam with both the central and one of the outer longitudinal reinforcement bars instrumented with DFOS. Fig. 10a shows the development of shrinkage induced deformation of these beams from the onset of drying. For

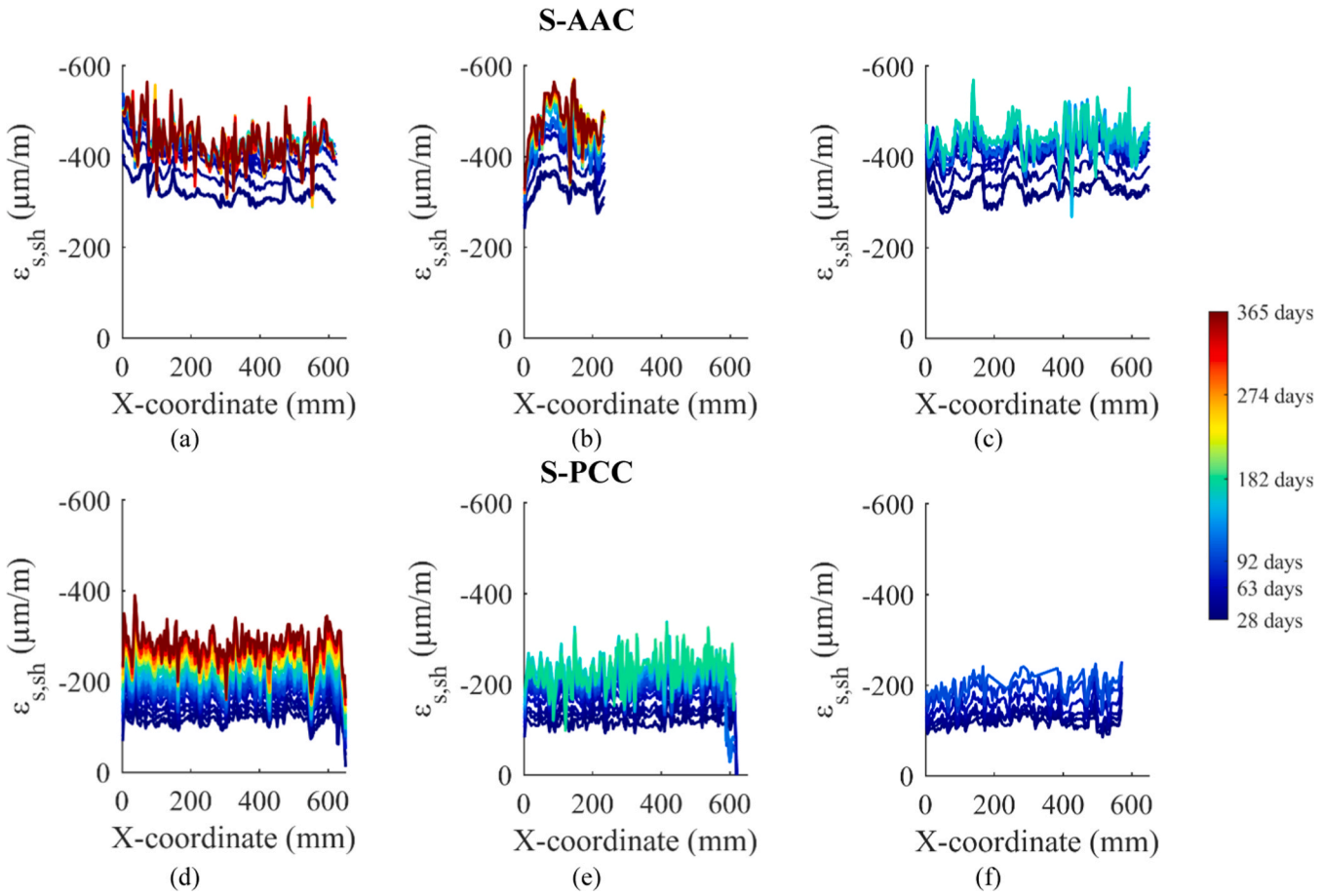

Fig. 8. Development of shrinkage induced steel strain for S-AAC replicates (a-c) and S-PCC replicates (d-f) over time.

comparison, the total plain concrete shrinkage (Fig. 5a) is also presented (from the onset of drying). Although drying rate is size dependent and plain concrete shrinkage was determined from a smaller cross-section (100×100 mm^2) than the reinforced concrete beams (150×200 mm^2), the difference between plain concrete shrinkage and shrinkage induced steel deformation is significantly larger in S-AAC than in S-PCC. For example, plain shrinkage of S-AAC reaches 350 μm/m at 92 days, while the corner reinforcement bar only deforms 140 μm/m. For S-PCC, this difference is significantly smaller; 220 μm/m plain shrinkage and 150 μm/m deformation of the corner bar at 92 days. This observation confirms that a significant portion of plain concrete shrinkage in GGBFS-based AACs could stem from creep. In addition, shrinkage-induced microcracking could amplify the difference between plain shrinkage and shrinkage induced deformations. As drying shrinkage is determined by the pore humidity gradient of concrete, it was anticipated that the outer bar would show a more rapid development of shrinkage induced deformations. However, unlike S-PCC, S-AAC shows a slower development of steel deformation in the outer longitudinal bar, which, due to hygral gradients, would be more susceptible to cracking than the central bar. To investigate the susceptibility to cracking, the side surfaces of the concrete beams are studied with an optical microscope at an age of 3 months. To highlight irregularities on the surface, the surfaces are wiped with a wet cloth. Figs. 10b and 10c show the side surface of S-AAC and S-PCC, respectively. From these figures it becomes evident that significant microcracks have formed on the surface of S-AAC. Note, also the bottom surface of S-AAC contained these microcracks. Although some microcracks were also observed in S-PCC, they have significantly smaller widths. Hence, S-AAC appears to be more susceptible to microcracking than S-PCC, which could explain the lower deformation of the outer reinforcement bar in S-AAC.

4. Conclusion

Development of concrete shrinkage induced deformations has been measured on embedded reinforcement bars instrumented with DFOS in reinforced GGBFS-based AAC and CEM III/B-based concrete beams and was compared to plain concrete shrinkage. The concretes have been fog-cured for 28 days and successively exposed to 20°C and 55 % relative humidity for a duration of 1 year. By combining bonded and unbonded DFOS strain measurements it was possible to decouple temperature effects and obtain mechanical steel strains induced by autogenous and drying shrinkage. As only the elastic part of plain concrete shrinkage can be imposed on reinforcement bars, it was possible to distinguish between the elastic and creep part in plain concrete shrinkage. Furthermore, DFOS provided quasi-continuous strain measurements along the reinforcement bar, which allowed to automatically detect local strain peaks and microcracks and determine their microcrack widths. Hence, DFOS provided useful insights in the complex shrinkage behavior of a novel concrete type, which could not have been captured from plain concrete shrinkage measurements. The following conclusions can be drawn from this study:

1) Autogenous shrinkage of plain GGBFS-based AAC develops rapidly and reaches 3 times larger deformations at 7 and 28 days compared to a CEM III/B-based concrete. The rapid development of autogenous shrinkage in GGBFS-based AAC can, at least partially, be attributed to the absence of autogenous expansion and rapid polymerization of GGBFS, leading to rapid strength development in the first 7 days. Furthermore, although the autogenous shrinkage development rate reduces after 3 months, autogenous shrinkage continued to develop

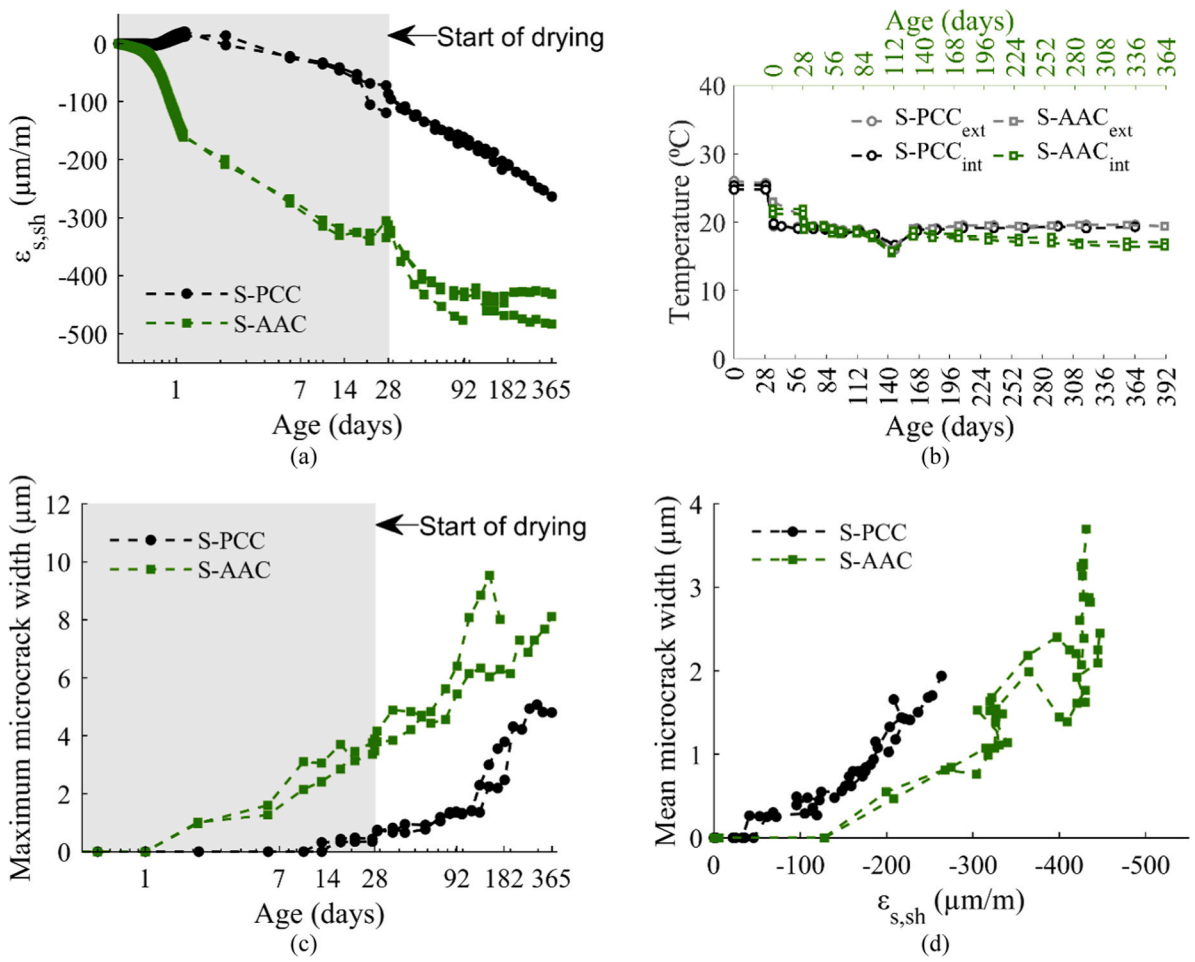

Fig. 9. Development of (a) mean shrinkage induced steel strain, (b) internal (int) and ambient (ext) temperature and (c) maximum microcrack width over time, and (d) relation between mean microcrack width and mean shrinkage induced steel strain.

in both concretes and significantly contributed to the total shrinkage of concrete.

2) Drying shrinkage of plain GGBFS-based AAC develops more rapidly, reaching 40 % larger values at 6 months, than in CEM III/B-based concrete. This can partially be attributed to the development of elastic compressive modulus over time, as GGBFS-based AAC shows a 10 % lower modulus at 28 days and a 25 % decline from 28 days to 1 year, compared to a CEM III/B-based concrete, which shows no significant variations in elastic compressive modulus from 28 days to 1 year.
3) GGBFS-based AAC shows a dormant period between 5 and 12 hours in its temperature evolution, while this is not observed in CEM III/B-concrete. In addition, GGBFS-based AAC reaches a higher (35 °C) peak temperature than CEM III/B-based concrete (32 °C).
4) GGBFS-based AAC shows a rapid development of autogenous shrinkage induced deformations at the end of its dormant period (9.5 hours after casting), which indicates significant stiffness gain of concrete and confirms the choice for a time-zero for shrinkage measurements in earlier studies [16]. Although CEM III/B-based concrete shows already development of autogenous expansion induced deformation 14 hours after casting, the expansion of steel is limited, confirming earlier studies on the choice for time-zero from the peak of expansion [45]. Unlike CEM III/B-based concrete, autogenous shrinkage induced deformations in GGBFS-based AAC started to develop slower than its plain shrinkage deformation after 52 hours, indicating that a significant portion of the autogenous shrinkage of GGBFS-based AACs could be creep. In addition, local microcracking along the reinforcement bar was detected and could have contributed.
5) Under drying, shrinkage induced deformations develop initially more rapidly for GGBFS-based AAC compared to CEM III/B-based concrete. However, the strain development rate in GGBFS-based AAC decreases after 56 days, while this was not evident for CEM III/B-based concrete. Although the effect of creep in plain concrete shrinkage cannot be ignored, the decrease in strain rate development might be amplified by opening of microcracks at the age of 56 days.
6) Local strain peaks along the reinforcement bar have been identified as microcracks. As shrinkage induced deformations increased, microcracks show to grow in number and width. GGBFS-based AAC shows already significant microcrack widths (>4 µm) under autogenous shrinkage induced deformations, while microcrack widths remain small (< 0.5 µm) in CEM III/B-based concrete. Unlike CEM III/B-based concrete, GGBFS-based AAC shows a rapid increase in microcrack width after 56 days, which is when shrinkage induced deformations stagnated, possibly explaining earlier observed decreases in stiffness and cracking resistance of reinforced GGBFS-based AAC members over time [11]. Similarly, the development of shrinkage induced deformations under drying developed slower in the outer reinforcement bar than the central reinforcement bar in GGBFS-based AAC, while the opposite and anticipated trend was observed in CEM III/B-based concrete. Microscopic images of the non-casted side surface of concrete beams confirmed the presence of microcracks and showed significantly larger microcrack widths for GGBFS-based AAC.

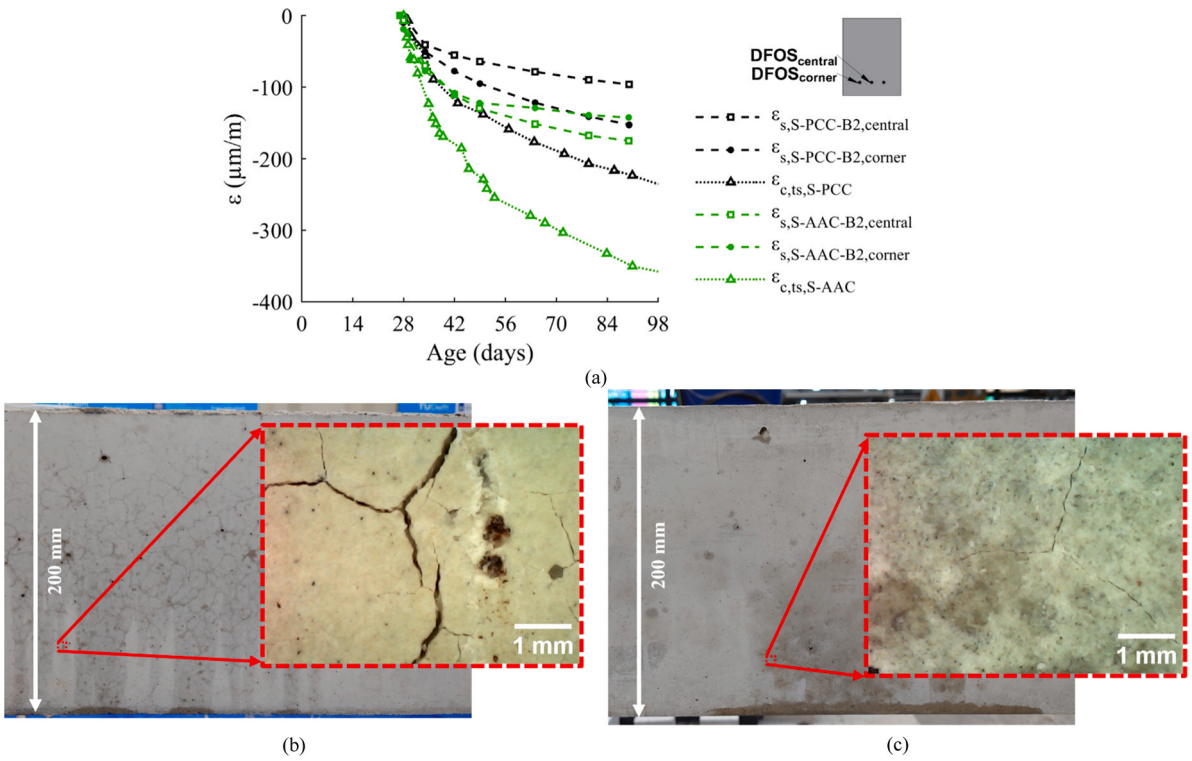

Fig. 10. (a) Development of mean shrinkage induced steel strain for beams exposed to drying (t_0=28 days) with a DFOS instrumented on the central and outer reinforcement bar, (b) surface cracks on non-casted side of S-AAC beam 2 (S-AAC-B2) and (c) S-PCC beam 2 (S-PCC-B2) at an age of 3 months.

It is important to note that the current study focuses on a specific GGBFS-based AAC and compares the results with a CEM III/B-based concrete under specific curing (>95 % RH) and exposure conditions (55 % RH and 20°C). Adopting a different alkaline activator, type of binder and/or exposure environment might lead to different results. Therefore, it is encouraged to focus on different curing regimes, binder compositions, activators and exposure conditions in future studies. As the current study was limited to the development of shrinkage induced steel deformation, future studies would need to investigate its implications to the structural behavior of GGBFS-based AACs under short-term and sustained loads. Furthermore, as the current study could not directly couple plain (drying) shrinkage to shrinkage induced deformations due to the effect of microcracking, creep, bending (due to asymmetric reinforcement) and size effects in drying, it is encouraged to investigate modelling strategies to decouple these effects.

Declaration of Competing Interest

The authors declare that they have no known competing financial interests or personal relationships that could have appeared to influence the work reported in this paper.

Acknowledgements

This work is supported by the AshCycle project, which is funded by the European Union (Grant number 101058162). The authors would like to express their gratitude for the obtained lab support.

Data availability

Underlying data is available at 4TU:
Data underlying publication: "Early-age and long-term deformations in reinforced slag-based alkali activated concrete" ()

References

[1] S. Venghaus, M. Henseleit, M. Belka, The impact of climate change awareness on behavioral changes in Germany: changing minds or changing behavior? Energy, Sustain. Soc. 12 (1) (2022).
[2] A. Leiserowitz, E. Maibach, S. Rosenthal, J. Kotcher, P. Bergquist, M. Ballew, M. Goldberg, A. Gustafson, X. Wang, Climate Change in the American Mind: April 2020, Yale Program on Climate Change Communication (2020).
[3] D.N. Huntzinger, T.D. Eatmon, A life-cycle assessment of Portland cement manufacturing: comparing the traditional process with alternative technologies, J. Clean. Prod. 17 (7) (2009) 668–675.
[4] S.A. Miller, A. Horvath, P.J.M. Monteiro, Readily implementable techniques can cut annual CO2-emissions from the production of concrete by over 20, Environ. Res. Lett. 11 (7) (2016).
[5] K.L. Scrivener, R.J. Kirkpatrick, Innovation in use and research on cementitious material, Cem. Concr. Res. 38 (2) (2008) 128–136.
[6] I.E.A., Technology Roadmap - Low-Carbon Transition in the Cement Industry, IEA, Paris, 2018.
[7] K.-H. Yang, J.-K. Song, K.-I. Song, Assessment of CO2 reduction of alkali-activated concrete, J. Clean. Prod. 39 (2013) 265–272.
[8] G. Kaklauskas, V. Gribniak, D. Bacinskas, P. Vainiunas, Shrinkage influence on tension stiffening in concrete members, Eng. Struct. 31 (6) (2009) 1305–1312.
[9] M.B. Davis, N.A. Hoult, S. Bajaj, E.C. Bentz, Distributed Sensing for Shrinkage and Tension Stiffening Measurement, Acids Struct. J. 114 (3) (2017).
[10] M.F. Bado, J.R. Casas, A. Dey, C.G. Berrocal, G. Kaklauskas, I. Fernandez, R. Rempling, Characterization of concrete shrinkage induced strains in internally-restrained RC structures by distributed optical fiber sensing, Cem. Concr. Compos. 120 (2021).
[11] H.J. Bezemer, N. Awasthy, M. Lukovic, Multiscale Analysis of Long-term Mechanical and Durability Behaviour of Two Alkali-activated Slag-based Types of Concrete, Constr. Build. Mater. 407 (2023).
[12] H. Ye, A. Radlińska, Shrinkage mechanisms of alkali-activated slag, Cem. Concr. Res. 88 (2016) 126–135.
[13] J. Ma, F. Dehn, Shrinkage and creep behavior of an alkali-activated slag concrete, Struct. Concr. 18 (5) (2017) 801–810.
[14] Z. Li, B. Delsaute, T. Lu, A. Kostiuchenko, S. Staquet, G. Ye, A comparative study on the mechanical properties, autogenous shrinkage and cracking proneness of alkali-activated concrete and ordinary Portland cement concrete, Constr. Build. Mater. 292 (2021).
[15] Z. Li, S. Zhang, X. Liang, G. Ye, Cracking potential of alkali-activated slag and fly ash concrete subjected to restrained autogenous shrinkage, Cem. Concr. Compos. 114 (2020).
[16] Z. Li, X. Liang, C. Liu, M. Liang, K. van Breugel, G. Ye, Thermal deformation and stress of alkali-activated slag concrete under semi-adiabatic condition: Experiments and simulations, Cem. Concr. Res. 159 (2022).

[17] D. Huang, P. Chen, H. Peng, Y. Yang, Q. Yuan, M. Su, A review and comparison study on drying shrinkage prediction between alkali-activated fly ash/slag and ordinary Portland cement, Constr. Build. Mater. 305 (2021).
[18] M. Hojati, F. Rajabipour, A. Radlińska, Drying shrinkage of alkali-activated cements: effect of humidity and curing temperature, Mater. Struct. 52 (6) (2019).
[19] A.M. Humad, J.L. Provis, K. Habermehl-Cwirzen, M. Rajczakowska, A. Cwirzen, Creep and Long-Term Properties of Alkali-Activated Swedish-Slag Concrete, J. Mater. Civ. Eng. 33 (2) (2021).
[20] F.G. Collins, J.G. Sanjayan, Workability and mechanical properties of alkali activated slag concrete, Cem. Concr. Res. 29 (1999) 455–458.
[21] M. Nedeljkovic, Carbonation mechanism of alkali-activated fly ash and slag materials in view of long-term performance predictions [doctoral dissertation], Tech. Univ. Delft, Delft (2019).
[22] I. Ismail, S.A. Bernal, J.L. Provis, S. Hamdan, J.S.J. van Deventer, Drying-induced changes in the structure of alkali-activated pastes, J. Mater. Sci. 48 (9) (2013) 3566–3577.
[23] T. Galkovski, J. Mata-Falcón, W. Kaufmann, Experimental investigation of bond and crack behaviour of reinforced concrete ties using distributed fibre optical sensing and digital image correlation, Eng. Struct. 292 (2023).
[24] R. Hoepffner, Distributed fiber optic strain sensing in hydraulic concrete and earth structures: Measuring theory and field investigations on dams and landslides, Tech. Univ. ät München (2008).
[25] X. Bao, L. Chen, Recent progress in distributed fiber optic sensors, Sens. (Basel) 12 (7) (2012) 8601–8639.
[26] Y. Lemcherreq, T. Galkovski, J. Mata-Falcon, W. Kaufmann, Application of Distributed Fibre Optical Sensing in Reinforced Concrete Elements Subjected to Monotonic and Cyclic Loading, Sensors 22 (5) (2022).
[27] O. Fischer, S. Thoma, S. Crepaz, Distributed fiber optic sensing for crack detection in concrete structures, Civ. Eng. Des. 1 (3-4) (2019) 97–105.
[28] T. Galkovski, Y. Lemcherreq, J. Mata-Falcon, W. Kaufmann, Fundamental Studies on the Use of Distributed Fibre Optical Sensing on Concrete and Reinforcing Bars, Sensors 21 (22) (2021).
[29] J.S. Yager, N.A. Hoult, E.C. Bentz, J.E. Woods, Measurement of Restrained and Unrestrained Shrinkage of Reinforced Concrete Using Distributed Fibre Optic Sensors, Sens. (Basel) 22 (23) (2022).
[30] M. Nedeljković, B. Ghiassi, S. van der Laan, Z. Li, G. Ye, Effect of curing conditions on the pore solution and carbonation resistance of alkali-activated fly ash and slag pastes, Cem. Concr. Res. 116 (2019) 146–158.
[31] NEN, Testing fresh concrete - Part 6: Density, NEN-EN 12350-6:2019, European Committee for Standardization, Brussels, 2019.
[32] NEN, Testing fresh concrete - Part 7: Air content - Pressure methods, NEN-EN 12350-7:2019, European Committee for Standardization, Brussels, 2019.
[33] NEN, Testing hardened concrete - Part 3: Compressive strength of test specimens, NEN-EN 12390-3:2019, European Committee for Standardization, Brussels, 2019.
[34] NEN, Testing hardened concrete - Part 13: Determination of secant modulus of elasticity in compression, NEN-EN 12390-13:2021, European Committee for Standardization, Brussels, 2021.
[35] F.Id Béton, fib Model Code for Concrete Structures (2020), fib, Lausanne Switzerland, 2023.
[36] NEN, Eurocode 2: Design of concrete structures - Part 1-1: General rules and rules for buildings, NEN-EN 1992-1-1+C2:2011 (NL), Europen Comittee for Standardization, Brussels, 2011.
[37] A.D. Kersey, M.A. Davis, H.J. Patrick, M. LeBlanc, K.P. Koo, C.G. Askins, M. A. Putnam, E.J. Friebele, Fiber grating sensors, J. Light. Technol. 15 (8) (1997) 1442–1463.
[38] H. Wang, Y. Liu, Z. Hu, H. Li, T. Yao, J. Liu, influencing aspects and mechanisms of steel bar reinforcement on shrinkage and cracking of cement-based materials, J. Build. Eng. 77 (2023) 107476.
[39] T. Janiak, H. Becks, B. Camps, M. Classen, J. Hegger, Evaluation of distributed fibre optic sensors in structural concrete, Mater. Struct. 56 (9) (2023).
[40] C.G. Berrocal, I. Fernandez, R. Rempling, Crack monitoring in reinforced concrete beams by distributed optical fiber sensors, Struct. Infrastruct. Eng. 17 (1) (2020) 124–139.
[41] F. Collins, J.G. Sanjayan, Effect of pore size distribution on drying shrinkage of alkali-activated slag concrete, Cem. Concr. Res. 30 (2000) 1401–1406.
[42] Z. Li, T. Lu, X. Liang, H. Dong, G. Ye, Mechanisms of autogenous shrinkage of alkali-activated slag and fly ash pastes, Cem. Concr. Res. 135 (2020).
[43] C. Cartwright, F. Rajabipour, A. Radlińska, Shrinkage Characteristics of Alkali-Activated Slag Cements, J. Mater. Civ. Eng. 27 (7) (2015).
[44] A.A.M. Neto, M.A. Cincotto, W. Repette, Drying and autogenous shrinkage of pastes and mortars with activated slag cement, Cem. Concr. Res. 38 (4) (2008) 565–574.
[45] M. Liang, Z. Chang, Y. Zhang, H. Cheng, S. He, E. Schlangen, B. Šavija, Autogenous deformation induced- stress evolution in high-volume GGBFS concrete: Macro-scale behavior and micro-scale origin, Constr. Build. Mater. 370 (2023).
[46] A. Darquennes, S. Staquet, M.-P. Delplancke-Ogletree, B. Espion, Effect of autogenous deformation on the cracking risk of slag cement concretes, Cem. Concr. Compos. 33 (3) (2011) 368–379.
[47] M. Nedeljkovic, Z. Li, G. Ye, Setting, Strength, and Autogenous Shrinkage of Alkali-Activated Fly Ash and Slag Pastes: Effect of Slag Content, Materials 11 (11) (2018).
[48] A. Wardhono, C. Gunasekara, D.W. Law, S. Setunge, Comparison of long term performance between alkali activated slag and fly ash geopolymer concretes, Constr. Build. Mater. 143 (2017) 272–279.
[49] S. Prinsse, D.A. Hordijk, G. Ye, P. Lagendijk, M. Luković, Time-dependent material properties and reinforced beams behavior of two alkali-activated types of concrete, Struct. Concr. 21 (2) (2019) 642–658.
[50] Kv Breugel, Invloed kruip op autogene krimp, Cement, 2023.
[51] D. H.E, Autogenous volume change of concrete, Proc. ASTM 40 (1940) 1002–1110.
[52] T.C. Powers, Mechanisms of shrinkage and reversible creep of hardening cement paste, Proc. Int. Symp. Struct. Concr. its Behav. Load. (1965) 319–344.
[53] B. Person, Creep and shrinkage of young or mature HPC, Proc. 5th Int. Symp. Util. High. strenght/High. Perform. Concr. (1999) 1272–1281.
[54] P. Lura, O.M. Jensen, J. Weiss, Cracking in cement paste induced by autogenous shrinkage, Mater. Struct. 42 (8) (2008) 1089–1099.
[55] Z. Li, T. Lu, Y. Chen, B. Wu, G. Ye, Prediction of the autogenous shrinkage and microcracking of alkali-activated slag and fly ash concrete, Cem. Concr. Compos. 117 (2021).
[56] A. Kostiuchenko, Creep of alkali-activated fly ash and slag concrete [doctoral dissertation], Materials and Environment, Delft Univeristy Technol., Delft (2024).
[57] F.G. Collins, J.G. Sanjayan, Microcracking and strength development of alkali activated slag concrete, Cem. Concr. Compos. 23 (2001) 345–352.